SUPPLEMENTARY INFORMATION

Resolving Intermediates during the Growth of Aluminum Deuteroxide (Hydroxide) Polymorphs in High Chemical Potential Solutions

Hsiu-Wen Wang[1], Emily T. Nienhuis[2], Trent R. Graham[2], Maxime Pouvreau[2], Jacob G. Reynolds[3], Mark Bowden[2], Gregory K. Schenter[2], James J. De Yoreo[2,4], Kevin M. Rosso[2], Carolyn I. Pearce[2,5]

[1] Chemical Sciences Division, Oak Ridge National Laboratory, Oak Ridge, Tennessee 37831, United States

[2] Pacific Northwest National Laboratory, Richland, Washington 99352, United States

[3] Washington River Protection Solutions, LLC, Richland, Washington 99352, United States

[4] Department of Materials Science and Engineering, University of Washington, Seattle, Washington 98195, United States

[5] Department of Crop and Soil Sciences, Washington State University, Pullman, Washington 99164, United States

This document contains:
Figures S1-S10
Texts (Sections 1-4)

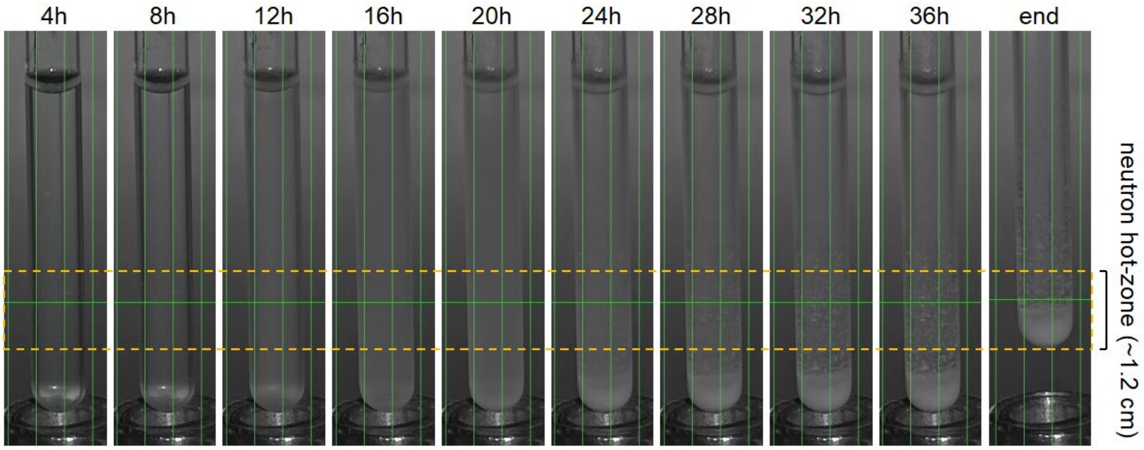

Figure S1. The infrared images captured during the neutron total scattering experiments, showing homogeneous nucleation and growth events for a period of 36 hours. The last image, marked as end, was taken at the end of the experiments with the sample position shifted upwards, so as the bottom of the tube is within the hot-zone of neutron beams. Yellow dashed box outlines the size of neutron hot-zone.

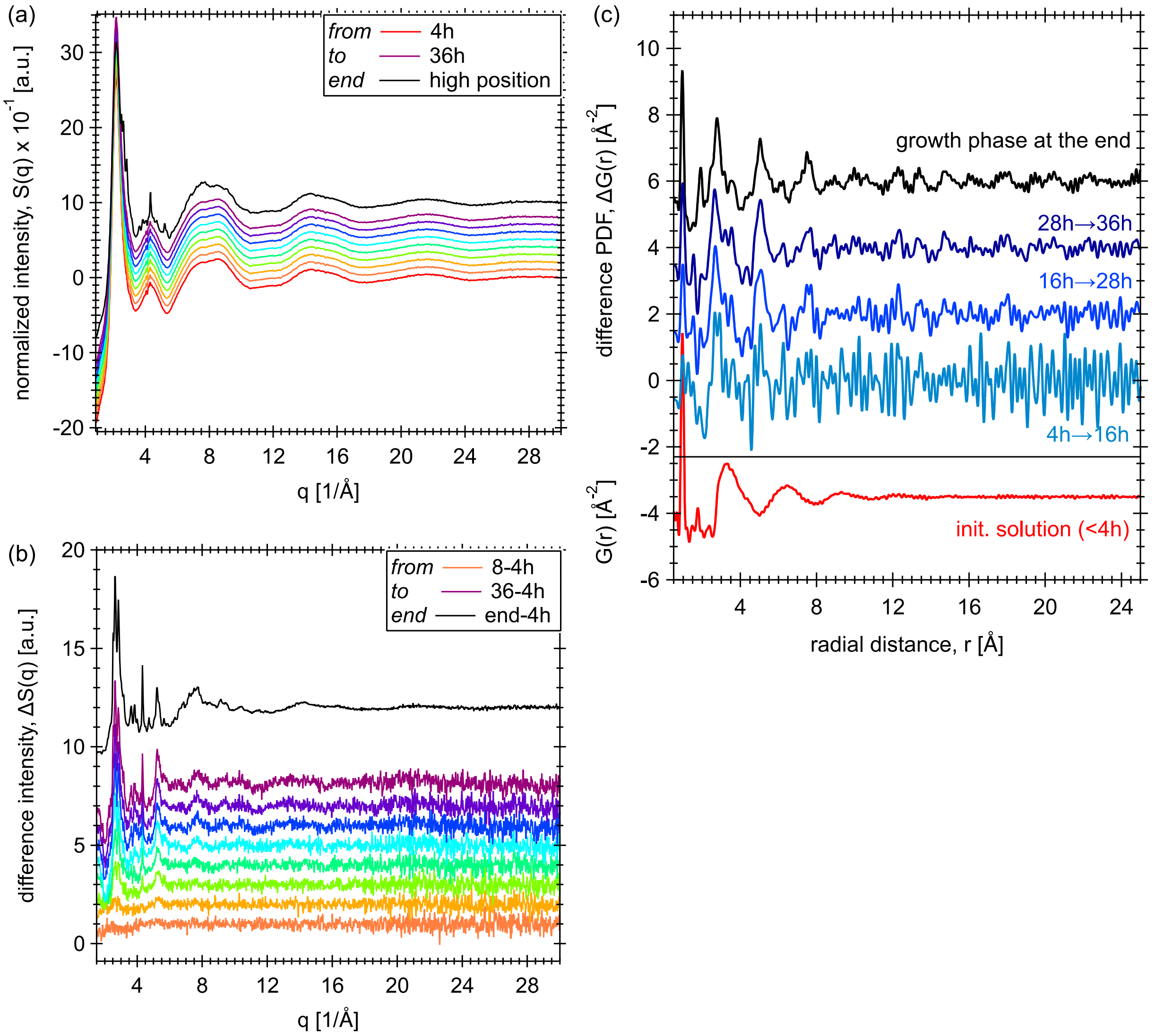

Figure S2. (a) In-situ neutron total scattering data following the nucleation and growth reactions of aluminum deutroxide(s). The S(q) dataset is offset by +1 in the y-axis for clarity. Corresponding infrared camera images captured during the measurements are shown in Figure S1. (b) Difference ΔS(q) curves every 4 hours relative to the first 4 hours dataset, showing the reaction progression as indicated by increasing peak intensities. The ΔS(q) dataset is offset by +1 in the y-axis for clarity. (c) Averaged difference PDF ΔG(r) datasets (blues and black curves) obtained at four different time intervals. The ΔG(r) dataset is offset by +2 in the y-axis for clarity. The PDF of the initial solution structure (completed at/within 4 hours after the solution was made) is shown by the red curve in the bottom panel.

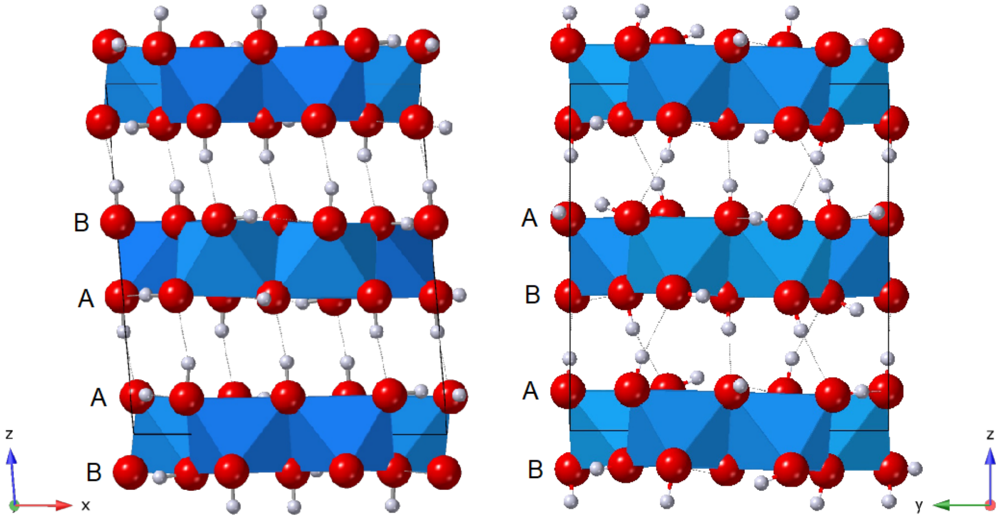

(a) **Gibbsite ($P2_1/n$):** the layer is stacked along the [001] direction, with adjacent layers rotated by a parallel twofold axis

(b) **Bayerite ($P2_1/n$):** the layer is stacked along the [001] direction, with adjacent layers related by an *n* glide plane

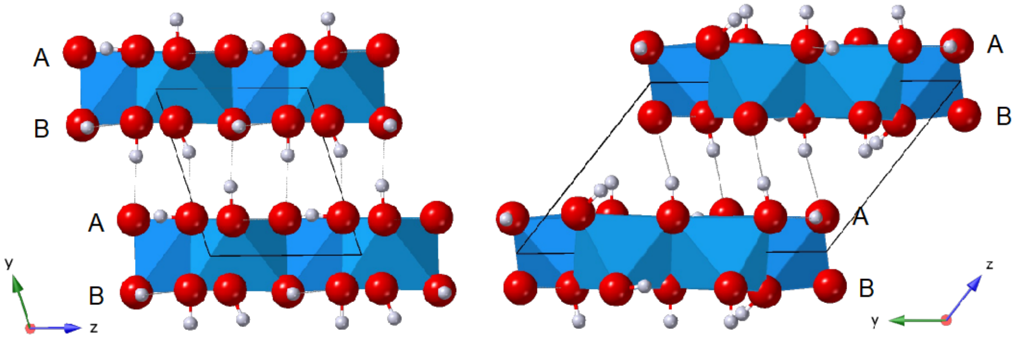

(c) **Dolyeite ($P1$):** the layer is stacked along the [010] direction, with adjacent layers simply translated by lattice vector

(d) **Nordstrandite (P-1):** the layer is stacked along the [001] direction, with adjacent layers simply translated by lattice vector

Figure S3. Projections of the crystal structure of (a) gibbsite, (b) bayerite, (c) dolyeite and (d) nordstrandite. These crystal structure data are from Balan *et al.*[1] for gibbsite, Zigan *et al.*[2] for bayerite, and Demichelis *et al.*[3] for doyleite and nordstrandit. O atoms are shown as red spheres, D as white spheres, and Al as blue octahedra. Unit cell is outlined by black box and interlayer D-bonds are shown as dashed lines. The A and B sites for the surface terminal -OD groups are also indicated.

Section 1: A single two-dimensional $Al(OD)_3$ layer model:

The model is consist of an isolated $Al(OD)_3$ layer created from gibbsite structure[1] with a unit cell of a = 8.742 Å, b = 5.112 Å, and c = 80 Å, i.e., layers of the type that compose gibbsite but the distance between layers were expanded such that there were no interlayer atom-atom correlations with the r-range being modeled (up to 30 Å). Structure model was refined against the PDF $\Delta G(r)$ data within PDFgui software[4]. During the fit we varied the overall scale factor, the unit cell, and the thermal displacements (U_{iso}) for Al, O, and D atoms. Spherical size damping parameter was not applied, because the uncertainties in the refined parameter were too large to reliably identify the size distributions. To correct the wrong baseline due to an enlarged unit cell setting, a dummy, low number density phase was added (as a two-phase modeling approach) to approximate baseline mismatches following the method described by Chen *et al.*[5] The fit r-range was 0.01-30 Å, and q_{damp}, q_{broad}, and q_{max} values were fixed during the refinements. After several refinement cycles, a suitable fit was obtained (Fig. 2 in the main text, $R_w = 0.35$). With all the atomic positions fixed, we observed about 1% decreasing in unit cell dimensions, and a relatively large U_{iso} value for D atoms (0.05±0.02 Å^2) compared to U_{iso} for Al (0.005±0.002 Å^2) and O (0.008±0.001 Å^2) atoms.

Comparison between the residual to the single layer model fit data and the calculated interlayer correlations was made via multiplying a scale factor of 0.1 to the four interlayer $G(r)$ curves shown in Figure S4c (described in Section 2 below). The results are displayed in Figure 2b in the main text, and R_w values are calculated for every 5 Å segments of the residual data.

Section 2: $Al(OD)_3$ bulk structure PDF calculations and modeling:

Figure S4 illustrates calculated total and partial neutron PDF G(*r*) of the four $Al(OD)_3$ polymorphs shown in Figure S3. The two partial PDFs are intralayer atom-atom correlation G(*r*) and interlayer atom-atom correlation G(*r*), respectively. The total G(*r*) is simply a linear summation of the two partial correlations. We found it useful to describe structure of $Al(OD)_3$ polymorphs in terms of these two partial correlations. Since they all share the same layer structure, despite the fact that D atoms are oriented differently in these polymorphs (Fig. S3), the corresponding intralayer G(*r*) are quite similar to each other (Fig. S4b). In contrast, the interlayer G(*r*) are very different (Fig. S4c), reflecting different modes of layer stacking. Also note that in all four calculated total G(*r*), at distances below ~6 Å, the total intensity is dominated mostly by the intralayer correlations.

An attempt of fitting observed PDF ΔG(*r*) data obtained at end of the neutron experiment using either gibbsite or bayerite bulk structures was also performed (Fig. S5). Refinements were performed using PDFgui software[4]. During the fit, all the atomic positions were fixed, but the unit cell dimensions and U_{iso} values for Al, O, and D atoms were refined. With q_{damp}, q_{broad}, and q_{max} parameters set up the same as in the single layer model fit, we found fits, over distances of 30 Å, were not matched to the features of either gibbsite or bayerite structural models. Interestingly, gibbsite model showed a slight better agreement to the experimental data than bayerite model (Fig. S5). In gibbsite structure, layers are stacked in a sequence of ABBA pattern, while in bayerite structure, the sequence is ABAB (Fig. S3). The differences in these two stacking patterns are reflected by their interlayer G(*r*) patterns, where the interlayer correlation of bayerite is stronger (with more ordered oscillating features) than that in gibbsite (Fig. S4c). Thus, a poor fit of bayerite model (Fig. S5b) is a result of "imbalanced" contributions between the intralayer and interlayer components, which together cannot be taken into account the whole *r*-range features efficiently. In gibbsite model, a better "balance" is achieved between the two partials (Fig. S5a), due to a weaker (less ordered) interlayer correlation in gibbsite structure. Therefore, attempt of fitting observed PDF ΔG(*r*) data with bulk structure suggests that a model with no (or weaker) contribution from interlayer correlation, such as a single two-dimensional $Al(OD)_3$ layer, is needed in order to properly explain the PDF ΔG(*r*) data observed at the end of the in-situ neutron experiment.

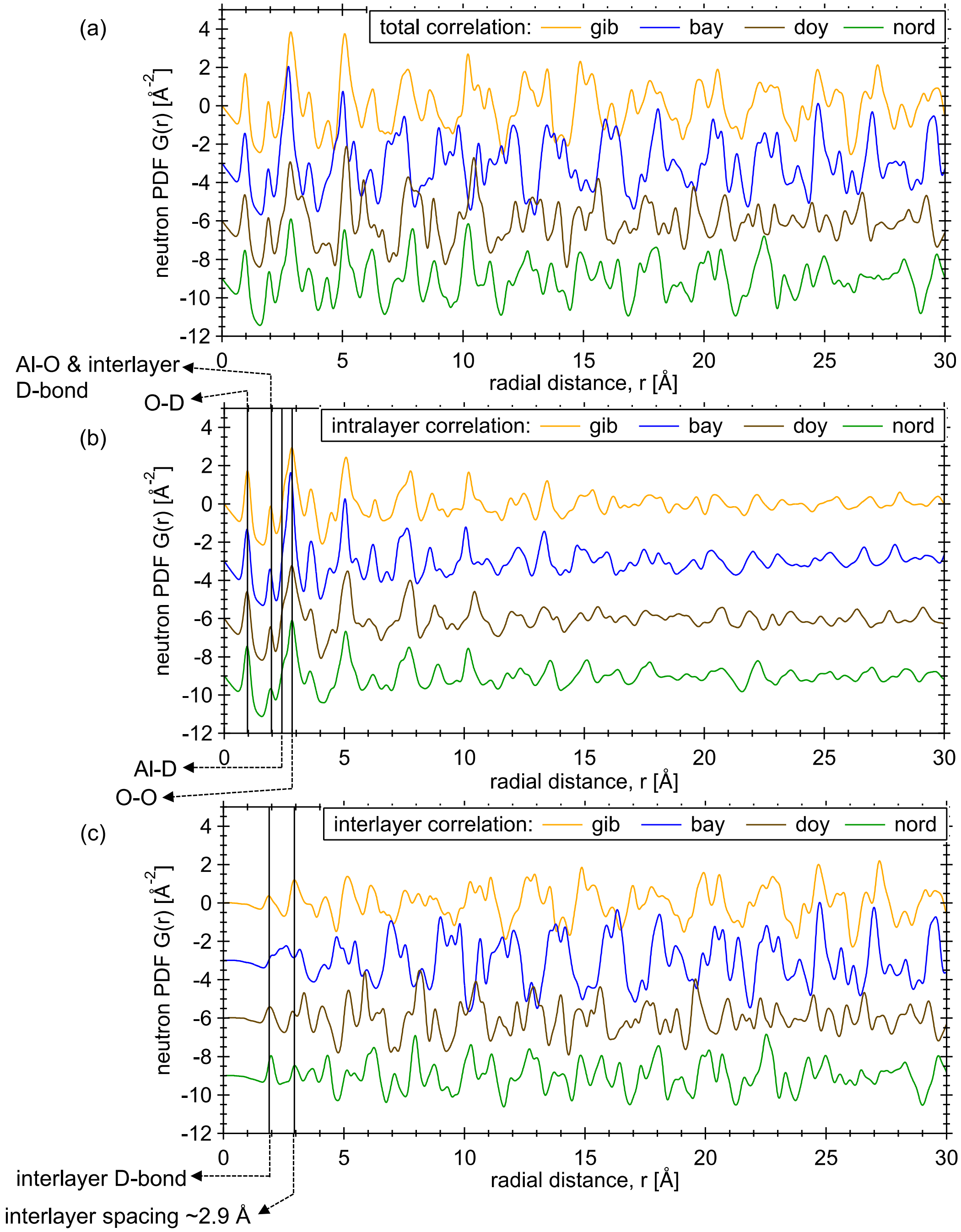

Figure S4. Simulated neutron (a) total PDF G(*r*) and (b-c) partial PDF G(*r*) of the four $Al(OD)_3$ polymorphs illustrated in Figure S3. Here, total G(*r*) = intralayer G(*r*) + interlayer G(*r*). Note that all intralayer correlations are similar with each other, despite the fact that D atoms are oriented differently in these polymorphs. The interlayer correlations, in contrast, are very different, reflecting different modes of layer stacking.

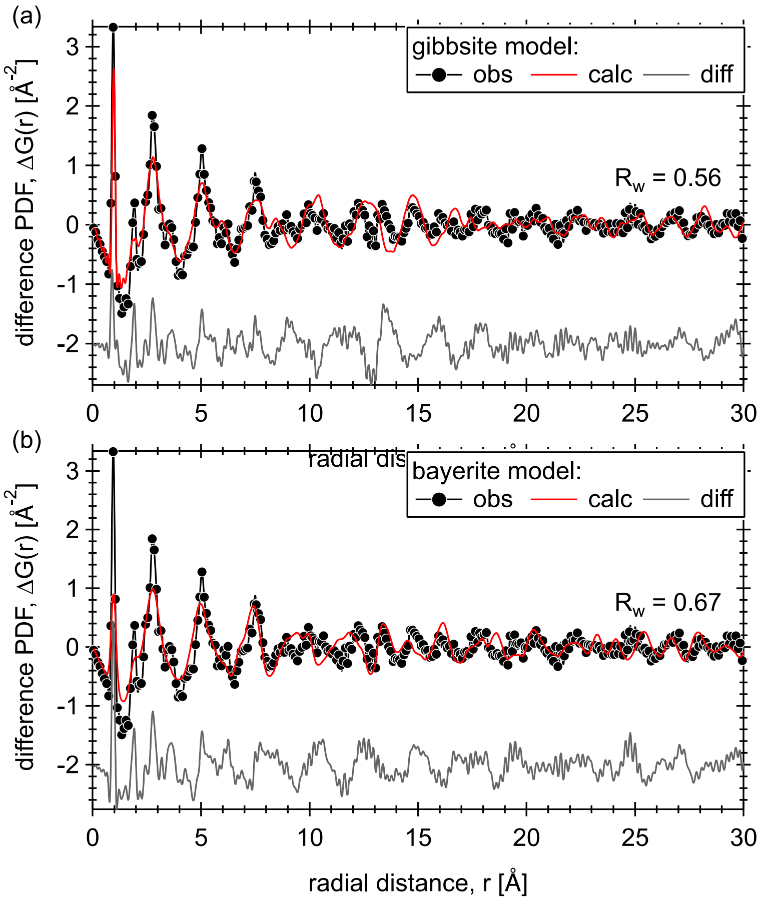

Figure S5. Poor fits of (a) gibbsite and (b) bayerite structural model to the observed PDF Δ G(*r*) data obtained at the end of the in-situ neutron experiment.

Section 3: ^{27}Al magic angle spinning nuclear magnetic resonance spectroscopy:

In-situ ^{27}Al magic angle spinning nuclear magnetic resonance (MAS NMR) spectra were acquired on an 11.7467 T NMR spectrometer using a 7.5 mm HX probe at ~20°C and a spinning rate of 100 Hz. The initial homogeneous solution was added to a WHiMS-style[6] rotor capable of containing suspensions under MAS conditions. Stable spinning was limited to around 100 Hz. The ^{27}Al MAS NMR spectra were acquired with a short tip angle ($\pi/20$), calibrated using a 1 M aluminum nitrate ($Al(NO_3)_3 \cdot 9H2O$, ≥98%, Sigma-Aldrich) solution in H_2O, which also served to calibrate the chemical shift axis (0 ppm). Other acquisition parameters included an acquisition time of 0.0102 s with 8533 complex points, a recycle delay of 5 s, and the collection of 2048 transients. Post-acquisition processing was performed in Mestrenova, where the free induction decay was zero-filled to 32k complex points, and 200 Hz of exponential line broadening was applied. The relative integral of the octahedral phase was estimated via deconvolution of the spectra using two purely Lorentzian line shapes, after correcting for probe ringing using the Whitaker smoother routine in Mestrenova. Figure S6 displays results of ^{27}Al MAS NMR spectra observed in situ over two weeks period.

Ex-situ ^{27}Al MAS NMR spectra were obtained with a Bruker NMR spectrometer at a field strength of 14.1 T. This field strength corresponds with a 156.375 MHz Larmor frequency for ^{27}Al. The single pulse direct excitation and triple quantum MAS NMR spectra were acquired with a MASDVT600W2 BL2.5 X/Y/H probe operating in dual resonance mode. The samples were loaded into commercial 2.5 mm rotors (Bruker), equipped with Vespel drive and bottom caps in an N_2-filled glovebox. The MAS spin rate was 20 kHz. The single-pulse, direct excitation ^{27}Al MAS NMR spectra were acquired with at least 8192 transients, with an acquisition time of 9.8 ms, a delay between transients of 0.5 s, and a single, $\pi/20$ liquid-state pulse of about 0.43 μs. The tip angles were based on pulse width nutation experiments prepared via dissolution of aluminum chloride hexahydrate ($AlCl_3 \cdot 6H_2O$, >99%, Sigma-Aldrich) in H_2O, and the chemical shifts are also referenced to this sample (0 ppm). ^{27}Al triple quantum MAS (3QMAS) NMR spectra were acquired at a field strength 14.1 T using a 2.5 mm MAS probe with the z-filter, ^{27}Al 3QMAS pulse sequence (mp3qzqf). The optimized pulse widths, p1, p2, and pw3s, were approximately 4.4, 1.7, and 17 μs, respectively. The time between the second and third pulses was 20 μs. The recycle delay (d1) was 2 s, and spectra were acquired with up to 256 evolution increments, a 14.88 ms acquisition time, and with between 108 and 720 transients, depending on the sample. The spectral widths for the F1 and F2 dimensions were 37.5 and 20.0 kHz, respectively. The acquired spectrum was processed with 100 Hz of exponential line broadening in the F2 dimension and displayed after shearing. Results of ex-situ ^{27}Al MAS NMR spectra are shown in Figures 3-5 in the main text.

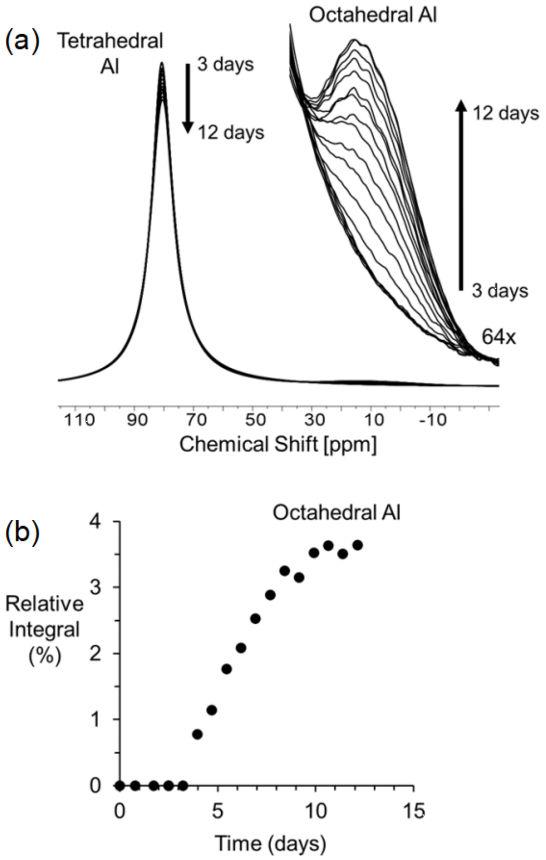

Figure S6. (a) Superimposed ^{27}Al MAS NMR spectra acquired at a field strength of 11.7467 T with an approximate spinning rate of 100 Hz. (b) Estimation of the numerical integral via deconvolutions using purely Lorentzian line shapes. Note that while ^{27}Al exhibits quadrupolar line shapes in solids, at these slow spinning speeds, the resonances attributed to octahedral Al in gibbsite and bayerite appear as a single quasi-Lorentzian resonance with a peak maximum at approximately 10 ppm. The Lorentzian deconvolution was used only for the estimation of the octahedral content. Readers are advised to refer to the reference[7] for the quadrupolar line shape parameters of bayerite, gibbsite, and other aluminum hydroxides, aluminum oxyhydroxides and alumina phases.

Section 4: X-ray Rietveld-internal standard refinements:

Powder X-ray diffraction was performed on a Rigaku SmartLab SE diffractometer using Cu-Kα radiation (λ = 1.5418 Å) with generator settings of 44 mA and 40 keV. Data were obtained at a scan rate of 0.9 °2θ/min with a step size of 0.01° from 2-100 °2θ using a position-sensitive D/teX ultra-detector with 250 individual detection elements. For all five post-precipitation samples (Fig. S7: three vacuum-filtrated samples collected at time points of 6 days, 45 days, and 3 months; and two samples with additional D_2O or ETOD washing after vacuum filtration of the 3-months precipitates), quantification of an amorphous fraction was conducted, using 10 wt.% rutile (TiO_2 standard reference material #674) as added crystalline internal standard. Rutile was selected as an internal standard as it minimized peak overlap with gibbsite and bayerite. To ensure homogenous distribution of the rutile standard and to minimize CO_2 adsorption, the sample and standard were mixed in an agate mortar and pestle in an N_2 glovebox. The vacuum filtered samples (collected at 6 days, 45 days, and 3 months) were loaded into an atmosphere-protected holder (zero-background circular cavity holder with an attached protective dome). The D_2O and ETOD washed samples were loaded into a standard zero-background circular cavity holder, instead of the atmosphere-protected holder, as the added D_2O and ETOD washing step generally resulted in less sensitivity to CO_2 adsorption.

The XRD pattern of the mixture was analyzed by Rietveld method using TOPAS Software (Bruker ASX). The starting structure models for gibbsite, bayerite, and monosodium aluminate hydrate (MSA; if presented) were adopted from Saalfeld *et al.*[8], Rothbauer *et al.*[9], and Kaduk *et al.*[10], respectively. Observations below 10 °2θ were excluded, since there are no observable diffraction peaks below 16 °2θ and to allow more simple background modelling. We used the Chebychev background function and profiles were modeled using a fundamental parameter description. Scale factor, specimen displacement, and specimen-related profile parameters were initially refined. Sources of peak broadening were analyzed by interpreting the Lorentzian coefficients refined in TOPAS, considering only crystallite size broadening. Preferred orientation was not modeled, and unit-cell parameters, atomic coordinates and isotropic displacement factors (B_{iso}) were not refined during the process of Rietveld refinement. The refined parameters had regular convergence and least-square R_{wp} factors, assessing the fitness of pattern, decreased gradually. The final R_{wp} values are 4.04%, 4.1 % and 2.90% for samples collected at 6 days, 45 days, and 3 months, respectively, and are 12.7% and 7.0% for the D_2O or

ETOD washed samples collected following vacuum filtration. Figure S8 depicts a selected 2θ range from Rietveld refinement results, and the determined phase abundance (in wt.%) is summarized in Table 1 of the main text. We noted that the poorer fits in the 6-days, 45-days, and the D_2O or ETOD washed samples are likely due to the complex disorder in gibbsite and bayerite phases. Although this can affect the accuracy of the quantitative analysis, modeling disorders are, however, beyond the scope of the current work. Disorder was not included in the model to avoid data overfitting and misinterpretation; therefore, our results are considered semi-quantitative within the scope of the work.

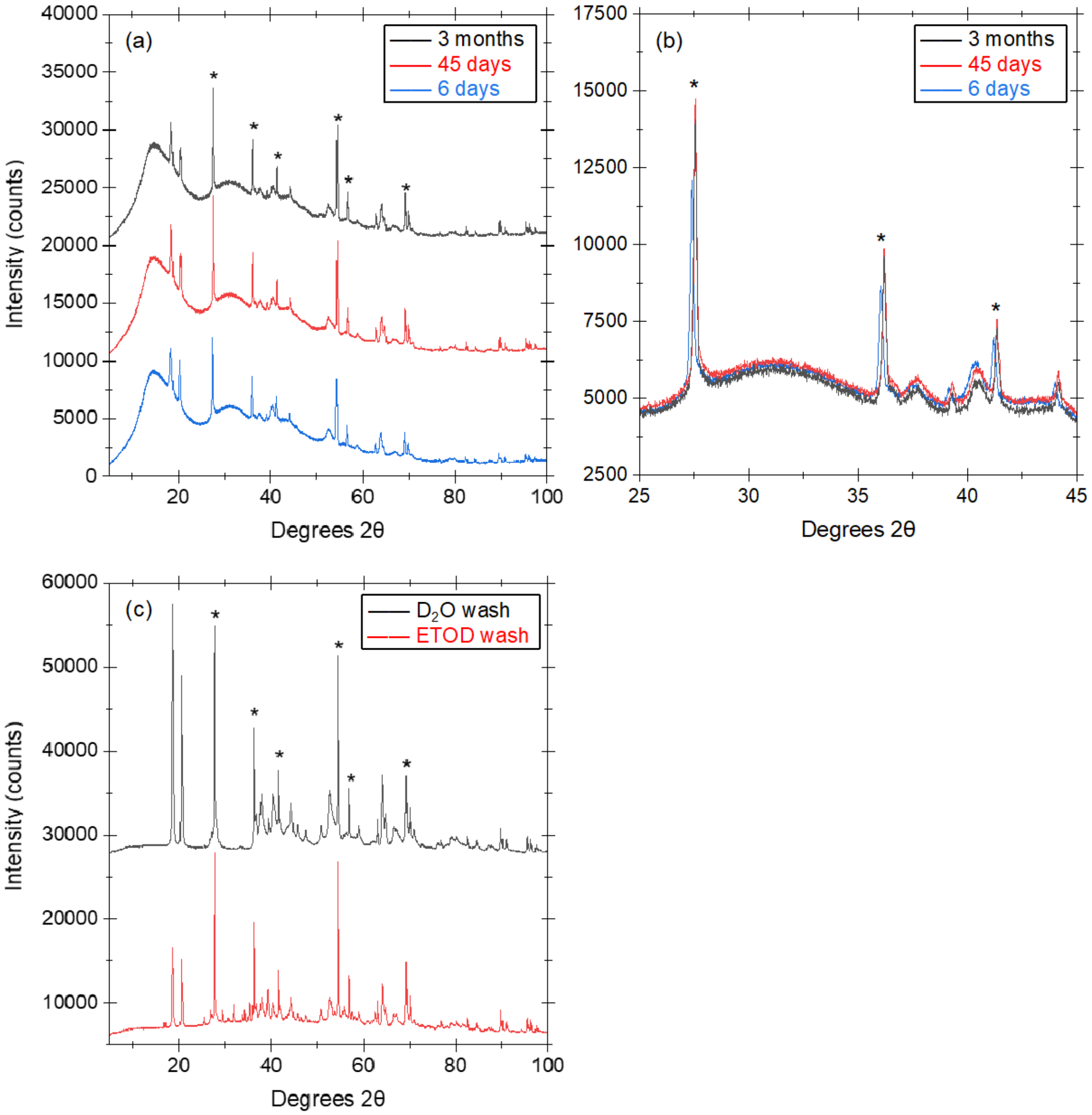

Figure S7. (a) XRD patterns of vacuum filtered samples collected at three different time points post precipitation: 6 days, 45 days, and 3 months. (b) A zoomed-in portion of plot a, showing smaller rutile peak intensities (asterisk symbol) in the 6-days sample. (c) XRD patterns of the D_2O or ETOD washed samples collected following vacuum filtration of the 3-months retrieved precipitates. In the plots a and c, data is offset in the *y*-axis for clarity. These samples were loaded into an atmospheric-controlled sample holder to prevent CO_2 adsorption, resulting in the increase of background intensity. Rutile (added as a 10 wt.% internal standard) reflections are denoted with an asterisk symbol. Because a fixed amount of rutile was added in each sample, smaller (and shifted) rutile peaks observed in the 6-days sample indicate a sample preparation error. Rietveld fits are shown in Figure S8.

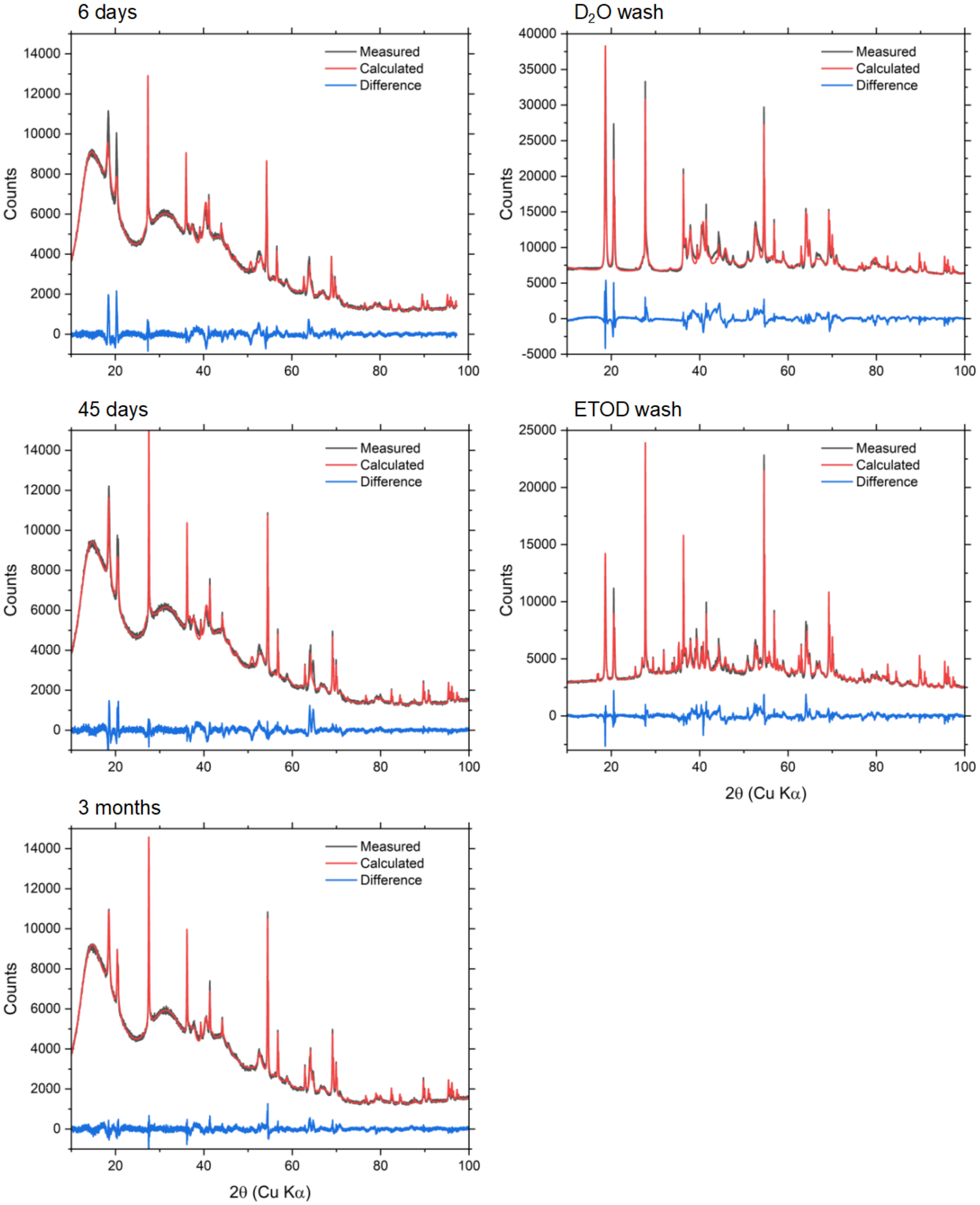
6 days

D$_2$O wash

45 days

ETOD wash

3 months

Figure S8. Rietveld refinement fits and residuals for the vacuum-filtrated solid samples collected at time points of 6 days, 45 days, and 3 months, and two samples with additional D_2O or ETOD washing after vacuum filtration of the 3-months precipitates. Note that these fits correspond to those reported in Figures S7a and S7b.

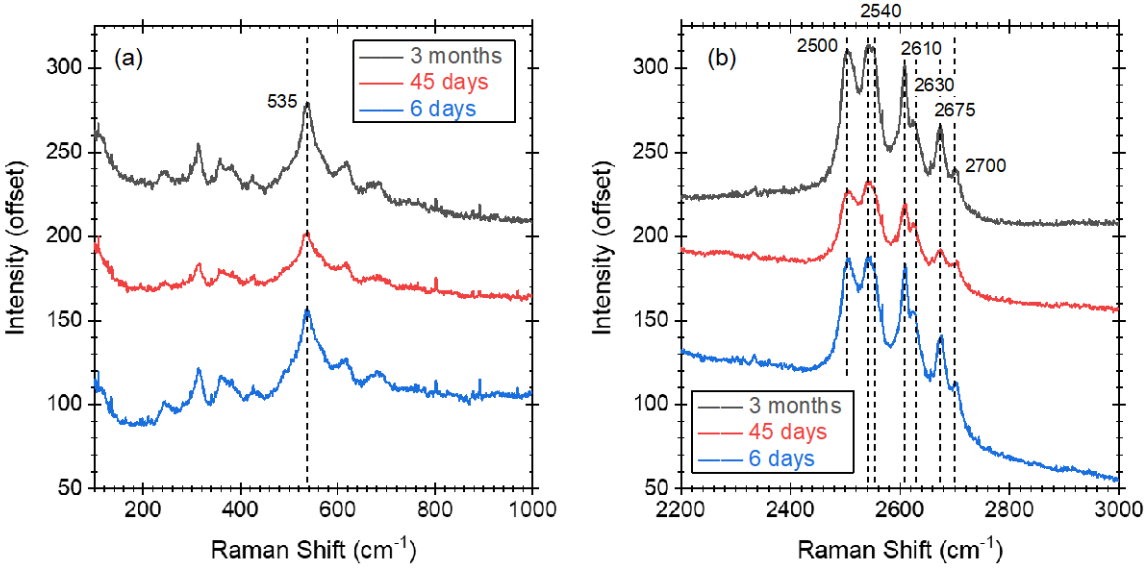

Figure S9. Raman spectra of the three time-series samples: 6 days, 45 days, and 3 months. (a) The low wavenumber region between 100-1000 cm^{-1} consists of AlOD librational bending, deformations, and Al-O-Al skeletal flexing vibrations. For example, the broad band centered at 535 cm^{-1} is typical attributed to Al-O-Al layer deformations in gibbsite and bayerite[11]. (b) The characteristic of the OD stretching modes in the range of 2200-300 cm^{-1}. Peak labelling indicates the proposed band allocation and assignment, taking a consideration of the mass differences in OD vs. OH for our deuterated precipitates. That is a scaling factor of 0.74 is applied to the predicted Raman-active OH stretching bands, based on works by Balan *et al.*[1,12] In general OD stretching bands of bayerite are similar to gibbsite but with an overall blueshift (move toward higher wavenumber) of the stretching bands[12]. Here, we observed four strong OD stretching bands at 2500, 2540, 2610, and 2675 cm^{-1} for gibbsite phase, and three major OD stretching bands at 2540, 2630, and 2700 cm^{-1} for bayerite phase. According to the theoretical mode assignments[1,12], the broader band centered at 2500 cm^{-1} (for gibbsite) and 2540 cm^{-1} (for gibbsite and bayerite) are from the significant coupling motion of the interlayer OD groups. In contrast, the narrower bands at 2610 and 2675 cm^{-1} (for gibbsite), and 2630 and 2700 cm^{-1} (for bayerite) are from the vibrations of intralayer OD groups, which are not coupled to each other. Note that the overall spectra intensity vary between samples as the spectra were not normalized and instead directly plotted for comparison.

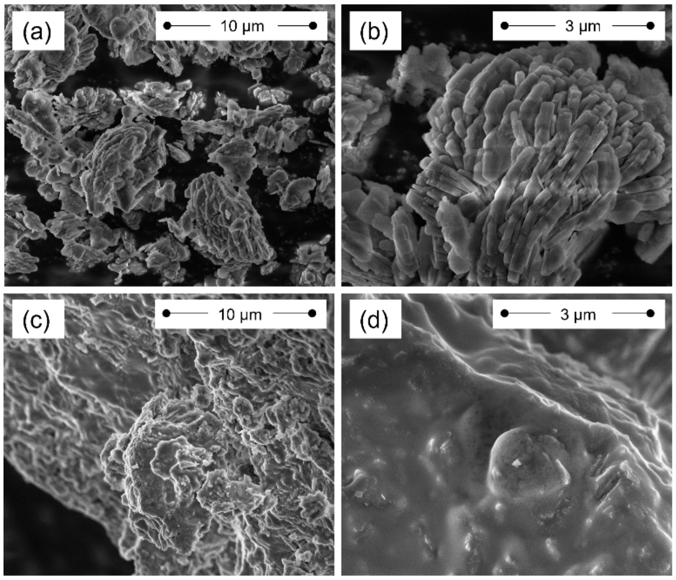

Figure S10. SEM images of precipitates collected, washed, and dried months after neutron experiment. (a-b) D_2O washed sample, and (c-d) ETOD washed sample. Note that these samples were not carbon coated for the measurement and the images show evidence of charging. These scanning electron micrographs were obtained with a Helios NanoLab SEM (FEI, Hillsboro, Oregon).

References

1 Balan, E., Lazzeri, M., Morin, G. & Mauri, F. First-principles study of the OH-stretching modes of gibbsite. *Am. Mineral.* **91**, 115-119 (2006).

2 Zigan, F., Joswig, W. & Burger, N. Die Wasserstoffpositionen im Bayerit, Al(OH)$_3$. *Z. Kristallogr. Cryst. Mater.* **148**, 255-274 (1978).

3 Demichelis, R., Catti, M. & Dovesi, R. Structure and Stability of the Al(OH)$_3$ Polymorphs Doyleite and Nordstrandite: A Quantum Mechanical ab Initio Study with the CRYSTAL06 Code. *J. Phys. Chem. C* **113**, 6785-6791 (2009).

4 Farrow, C. L. et al. PDFfit2 and PDFgui: computer programs for studying nanostructure in crystals. *J. Phys.: Condens. Matter* **19**, 335219 (2007).

5 Chen, Z., Beauvais, M. L. & Chapman, K. W. Pair distribution function analysis of discrete nanomaterials in PDFgui. *J. Appl. Crystallogr.* **56**, 328-337 (2023).

6 Walter, E. D. et al. Operando MAS NMR Reaction Studies at High Temperatures and Pressures. *J. Phys. Chem. C* **122**, 8209-8215 (2018).

7 Chandran, C. V. et al. Alumina: discriminative analysis using 3D correlation of solid-state NMR parameters. *Chem. Soc. Rev.* **48**, 134-156 (2019).

8 Saalfeld, H. & Wedde, M. Refinement of the crystal structure of gibbsite, A1(OH)$_3$. *Z. Kristallogr. Cryst. Mater.* **139**, 129-135 (1974).

9 Rothbauer, R., Zigan, F. & O'Daniel, H. Verfeinerung der Struktur des Bayerits, Al(OH)$_3$. *Z. Kristallogr. Cryst. Mater.* **125**, 317-331 (1967).

10 Kaduk, J. A. & Pei, S. The crystal structure of hydrated sodium aluminate, $NaAlO_2 \cdot 5/4H_2O$, and its dehydration product. *J. Solid State Chem.* **115**, 126-139 (1995).

11 Ruan, H. D., Frost, R. L. & Kloprogge, J. T. Comparison of Raman spectra in characterizing gibbsite, bayerite, diaspore and boehmite. *J. Raman Spectrosc.* **32**, 745-750 (2001).

12 Balan, E., Blanchard, M., Hochepied, J.-F. & Lazzeri, M. Surface modes in the infrared spectrum of hydrous minerals: the OH stretching modes of bayerite. *Phys. Chem. Miner.* **35**, 279-285 (2008).